Biophysical *Journal*
Article

Biophysical Society

Hydrodynamic Hunters

Hossein Jashnsaz,[1] Mohammed Al Juboori,[2] Corey Weistuch,[3,4] Nicholas Miller,[2] Tyler Nguyen,[5] Viktoria Meyerhoff,[6] Bryan McCoy,[7] Stephanie Perkins,[8] Ross Wallgren,[9] Bruce D. Ray,[1] Konstantinos Tsekouras,[1] Gregory G. Anderson,[8,*] and Steve Pressé[1,7,10,*]

[1]Department of Physics and [2]Biomedical Engineering, Indiana University - Purdue University Indianapolis (IUPUI), Indianapolis, Indiana; [3]Department of Applied Mathematics and Statistics and [4]Department of Biochemistry and Cell Biology, Stony Brook University, Stony Brook, New York; [5]Stark Neurosciences Research Institute, Indiana University School of Medicine (ISUM), Indianapolis, Indiana; [6]Mechanical Engineering, [7]Department of Chemistry and Chemical Biology, [8]Department of Biology, and [9]Department of Mathematical Sciences, Indiana University - Purdue University Indianapolis (IUPUI), Indianapolis, Indiana; and [10]Cellular and Integrative Physiology Department, Indiana University School of Medicine (IUSM), Indianapolis, Indiana

ABSTRACT The Gram-negative *Bdellovibrio bacteriovorus* (BV) is a model bacterial predator that hunts other bacteria and may serve as a living antibiotic. Despite over 50 years since its discovery, it is suggested that BV probably collides into its prey at random. It remains unclear to what degree, if any, BV uses chemical cues to target its prey. The targeted search problem by the predator for its prey in three dimensions is a difficult problem: it requires the predator to sensitively detect prey and forecast its mobile prey's future position on the basis of previously detected signal. Here instead we find that rather than chemically detecting prey, hydrodynamics forces BV into regions high in prey density, thereby improving its odds of a chance collision with prey and ultimately reducing BV's search space for prey. We do so by showing that BV's dynamics are strongly influenced by self-generated hydrodynamic flow fields forcing BV onto surfaces and, for large enough defects on surfaces, forcing BV in orbital motion around these defects. Key experimental controls and calculations recapitulate the hydrodynamic origin of these behaviors. While BV's prey (*Escherichia coli*) are too small to trap BV in hydrodynamic orbit, the prey are also susceptible to their own hydrodynamic fields, substantially confining them to surfaces and defects where mobile predator and prey density is now dramatically enhanced. Colocalization, driven by hydrodynamics, ultimately reduces BV's search space for prey from three to two dimensions (on surfaces) even down to a single dimension (around defects). We conclude that BV's search for individual prey remains random, as suggested in the literature, but confined, however—by generic hydrodynamic forces—to reduced dimensionality.

INTRODUCTION

The Gram-negative bacterium *Bdellovibrio bacteriovorus* (BV) (1) is a model bacterial predator found across diverse habitats (2). It is poised to help purify water and soil (3), degrade biofilms (4), and serve as a living antibiotic (5). Decades of research have elucidated many aspects of BV's behavior (1). BV has a biphasic life cycle that includes an attack phase and a free-living phase. During the attack phase, BV grows within its Gram-negative prey's periplasm, replicates and, in a dramatic lytic event reminiscent of a virus, releases its free-living (mobile) phase progeny in search of bacterial prey. Most recently, studies have identified factors involved in its attachment and entry into prey (6), its effectiveness in killing pathogens (4,5,7,8), and safety in animal models (9,10). The availability of BV's genome sequence (2) has spurred detailed study into BV's physiology and molecular regulation (11,12). Despite this work, it is still unknown whether BV specifically targets its Gram-negative prey or simply bumps into it at random (3,13–15).

Early bulk studies concluded that BV most likely collides with prey randomly in solution, showing no significant chemotactic response for prey concentrations below 10^8 cells/mL while, at higher prey concentrations, sensing of prey by BV was attributed to the lysis of prey cells (3,14). More recent studies have shown that chemotaxis plays a modest role, and that while BV infects some prey cells more efficiently than others (7), no single receptor on BV's prey has been identified as a point of attachment

Submitted November 2, 2016, and accepted for publication February 7, 2017.

*Correspondence: stevenpresse@gmail.com or ga2@iupui.edu

Nicholas Miller and Tyler Nguyen contributed equally to this work.

Viktoria Meyerhoff, Bryan McCoy, Stephanie Perkins, and Ross Wallgren contributed equally to this work.

Steve Presse's present address is Physics and School of Molecular Sciences, Arizona State University, Tempe, Arizona

Editor: Anatoly Kolomeisky.

http://dx.doi.org/10.1016/j.bpj.2017.02.011

(15). In fact, BV's attachment to *Salmonella spp.* and *Escherichia coli* is robust to various outer membrane mutants (15,16).

It is conceivable that BV's hunting strategy would appear random if it is receiving conflicting chemoattractant signals from multiple surrounding prey. However, when sufficiently close to any single prey, no distinctive statistical signature of a targeted (chemotactic) search by BV for its prey—for instance, a volcano (17) effect that is expected for predators sensing chemoattractant point sources—has been found (18). Chemical sensing by BV for its prey would require BV to sensitively detect its prey and perhaps even forecast its moving prey's future position.

On the other hand, it is known that bacteria respond to self-induced (19,20) as well as external (21) hydrodynamic flows. For example, *E. coli* shows flagellar-mediated circular motion due to self-induced hydrodynamic flows near surfaces (22–24) and swims counter to external flows (21). Our experimental results discussed below—recapitulated by hydrodynamic calculations—demonstrate that not only is fast moving BV strongly influenced by its own self-generated hydrodynamic fields, but that hydrodynamic effects are critical in allowing BV to locate its prey. Because BV is small (~0.5 μm) and swims rapidly (>50 μm/s) through solution, our results show that it violently perturbs its liquid environment. While the complex dynamical effects of the liquid environment's response have been widely investigated for inanimate microswimmers such as catalysts (25), the role of hydrodynamics in bacterial predator-prey interactions is new, to our knowledge.

MATERIALS AND METHODS

Media

Bacteria were grown in Nutrient Broth (NB: 1 g/L yeast extract, 5 g/L peptone, 3 g/L beef extract, 0.294 g/L $CaCl_2$, pH 7.6); Diluted Nutrient Broth (DNB: 0.1 g/L yeast extract, 0.5 g/L peptone, 0.3 g/L beef extract, 0.294 g/L $CaCl_2$, pH 7.6); or calcium HEPES (CaHEPES: 0.294 g/L $CaCl_2$, 5.94 g/L HEPES, pH 7.6), as indicated in the text.

E. coli culture

E. coli strain MG1655 (26,27) was grown overnight in NB at 37°C with shaking (180 rpm). For *E. coli* motility experiments, the culture was used within 1–3 h after removal from the shaker.

BV culture

We used *Bdellovibrio bacteriovorus* (BV) strain 109 (BV Stolp and Starr, ATTC No. 15143; American Type Culture Collection, Manassas, VA) for all experiments in this study, unless otherwise mentioned. Frozen BV stocks were thawed at room temperature, pelleted in a microcentrifuge at 10,000 rpm for 6 min, and resuspended in 3 mL CaHEPES. Cultures were incubated at 30°C for 3 h, fed with 1 mL 3-day-old *E. coli* (strain SM10) culture, then incubated again in the same conditions. BV motility experiments were done after 12 h.

Microscopy and tracking

Bacteria were imaged with an inverted microscope (Nikon, Melville, NY) using a 60× phase oil immersion objective. Forty-five-second videos were recorded and trajectories were manually tracked using NIS tracking software (Nikon). We ignored nonmobile bacteria everywhere. The bacteria often went in and out of focus due to z-plane motion. To restrict our tracking to specific planes, we stopped tracking when bacteria got slightly out of focus (± 1 μm within the focus plane). In Figs. 2 and 4 *B*, BV and *E. coli* were tracked only while in complete focus to ensure that trajectories represented bacteria on the exact focus plane (with an estimated error bar of $\Delta z \sim 1$ μm).

Sample preparation

To explore movement around beads, we used electrically neutral Sepharose CL-6B beads (cross-linked (CL) beads; Sigma-Aldrich, St. Louis, MO), electrically positive diethylaminoethyl (DEAE) Sepharose Fast Flow beads (DEAE beads; GE Healthcare Life Sciences, Marlborough, MA), and electrically negative Sulfopropyl (SP) Sepharose Fast Flow beads (SP beads; Sigma-Aldrich), with sizes (radii) of 5–150 μm. To prepare and add beads to slides with motile bacteria, 30 μL of bead stock solution was added to 1 mL CaHEPES in a microcentrifuge tube and was centrifuged at 6400 rpm for 5 min. The supernatant was then removed and CaHEPES was added to the beads up to 1 mL total in the microcentrifuge tube. These steps were repeated 2–3 times. After the third wash, beads were resuspended in 1 mL of DNB and added to the slides with DNB and motile bacteria solutions (1/3 beads, 1/3 DNB, 1/3 BV or *E. coli*). To construct walls, a drop of nitrocellulose polymer was sandwiched between a coverslip and a microscope slide. Under slight pressure of the coverslip, the polymer spreads (typical diameter ~0.5–2 cm). After curing, it forms a hard edge straight enough to be considered a wall on the length scale of an ~0.5 μm BV (or even ~1 μm *E. coli*). Healthy swimming BV or *E. coli* solutions were then introduced against the edge of the wall.

RESULTS AND DISCUSSION

Before investigating hydrodynamics, we first looked at the behavior of populations of active BV around individual *E. coli* as well as larger pellets of *E. coli* to study the effect of chemotaxis on BV's search for its prey. The results are shown in Fig. 1, which reveals no density enhancement (chemotaxis) of predator around an individual prey cell (Fig. 1, *A* and *B*). However, large chunks of prey cells chemotactically attracted BV (Fig. 1, *C* and *D*). Both of these results are in agreement with early bulk studies using chemotaxis assays suggesting that BV most likely collides with individual prey randomly in solution, showing no significant chemotactic response for prey concentrations below 10^8 cells/mL while, at higher prey concentrations, sensing of prey by BV was attributed to its probable attraction to cell lysate (3,14).

Next, to establish that BV is in fact influenced by its own self-generated hydrodynamic flow fields near surfaces, we monitored BV swimming parallel to flat surfaces (Fig. 2). As BV's single flagellum rotates, propelling its body forward, its body counterrotates. In doing so, we expect BV to generate hydrodynamic flows above and below its body consistent with what is known about microswimmers swimming parallel to flat surfaces while rotating along their long axis (19,22,24). In this circumstance, fluid friction at the

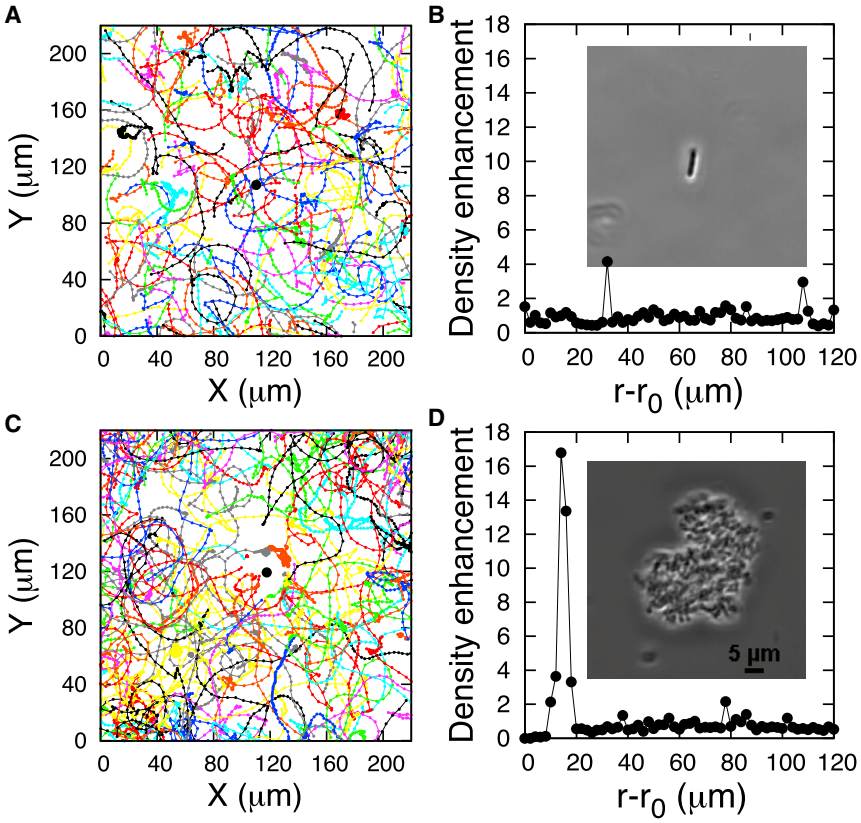

FIGURE 1 BV do not show chemotaxis toward individual *E. coli* although they do chemotactically accumulate around large chunks of *E. coli*. (*A*) Shows BV trajectories around an individual *E. coli* (whose location is designated by the *middle dot*). The density enhancement of BV is shown in (*B*) around the prey. (*C*) Shows the trajectories of BV around a large chunk of *E. coli*. The density enhancement of BV is shown in (*D*) around the chunk of prey. The insets in (*B*) and (*D*) show the microscope images of the individual *E. coli* and *E. coli* chunk; r_0 shows their geometric centers, respectively. The density enhancements in (*B*) is the density of motile BV with respect to the center of the individual *E. coli* computed at various distances from the *E. coli* divided by the average background density away from *E. coli* (see the Supporting Material for density calculation and Fig. S7). In (*D*), the only difference with (*B*) is that it is now the density of motile BV with respect to the geometric center of the chunk of *E. coli*. To create a chunk of *E. coli*, its overnight culture (see Materials and Methods) was centrifuged and the pellet suspended in CaHEPES, and a proper size piece of it was located under the microscope on a slide. To see this figure in color, go online.

surface (idealized as a no-slip boundary) induces a net force perpendicular to the swimmer's direction of motion. This, in turn, causes the swimmer to exhibit circular trajectories near surfaces. As we will discuss shortly, *E. coli* qualitatively behaves in the same way as BV although its flagellar physiology is completely different (*E. coli* has many flagella that bundle, while BV has just one). This suggests that the hydrodynamic forces described which act on the bacterium's body arise from the rotation of the body, not the details of the bacterial flagellar physiology.

In addition, we find that BV's trajectories show opposite helicities (clockwise versus counterclockwise rotation) on opposite surfaces (slide and coverslip, see Fig. 2 *A*) as would be expected if the circular trajectories were hydrodynamic in origin (Fig. 2, *B–H*; Movies S1, S2, and S3). Helicities are expected to switch if the flagellum predominantly rotates in one direction but the no-slip boundary condition is moved from below to above BV (see Fig. 2, *B* and *D*). Additionally, we confirmed that BV's flagellum rotates in one direction by monitoring BV tethered by its flagellum on a coverslip and tracking its body's rotation (Fig. S3).

While circular motion of bacteria may be caused by autochemotaxis (28), our data (Fig. 2, *B–H*) reveal a progressive loss of trajectory curvature as we move away from the surfaces and an eventual flip in helicity of BV's trajectories as we move past the midplane toward either the coverslip or the slide, consistent with hydrodynamic interactions and not autochemotaxis. Furthermore, by implementing a model presented in Spagnolie and Lauga (29) with boundary conditions consistent with those of our system, we can recapitulate both the helicity of the trajectory on surfaces and the increasing radius of curvature of those trajectories as we move away from the surface (Fig. 2 *J*); see Fig. S2 and the Supporting Material. Importantly, as we increase the viscosity of the solution, we saw the radius of the trajectories monotonically increase as would be expected if hydrodynamic effects weakened at higher viscosity (Fig. S4). While the component of the self-induced hydrodynamic flow parallel to the surface generates helicity in BV's trajectories near surfaces (22,24), the component perpendicular to the surface keeps bacteria close to the boundary, as shown in Fig. 2, *I* and *K*, where speed, dwell time, and length histograms show that hydrodynamics preferentially localize BV to regions near surfaces.

Many studies have investigated the accumulation of swimming microagents at flat surfaces including bacteria, algae, and artificial microswimmers (30–35). While this accumulation of microswimmers has been attributed to a number of different phenomena such as lubrication or near-field flows (25), persistent swimmer motion (34), or even contact interactions (32), our experimental results (Fig. 2), controls (Figs. S3 and S4), and numerical simulations (Fig. 2 *J*) discussed

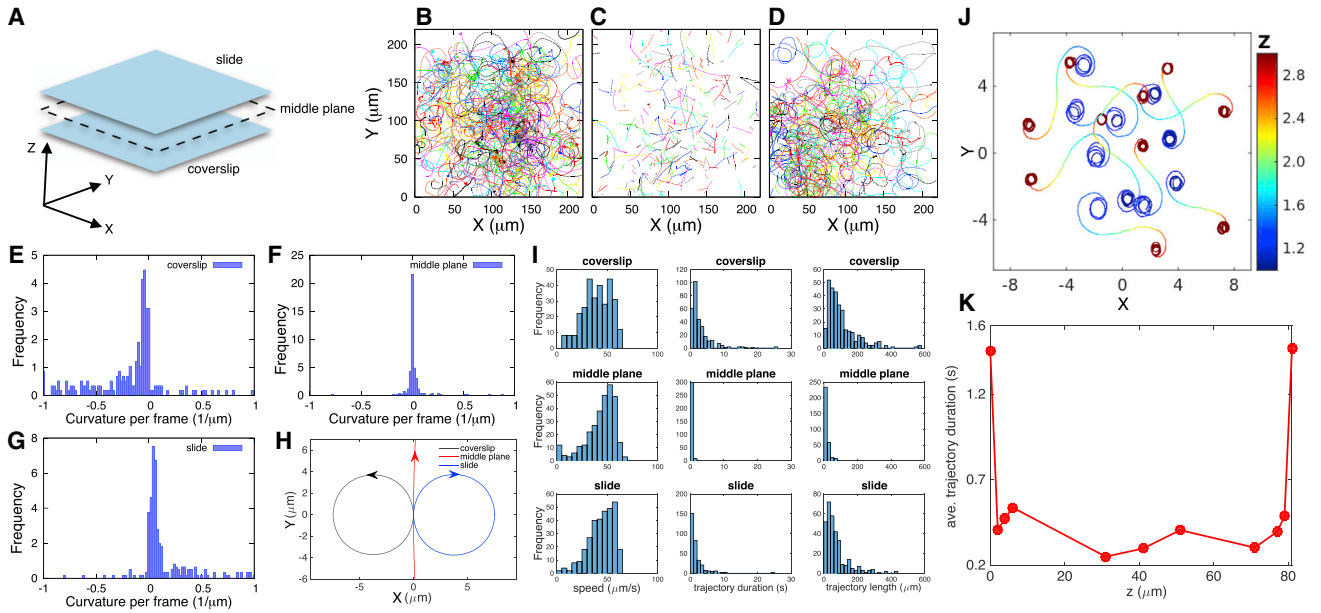

FIGURE 2 Self-generated hydrodynamic flows cause BV to interact strongly with surfaces. The motility of active BV was monitored at various planes between a microscope slide and a coverslip (*A*) separated by 40–90 μm (in such a way that the bacterium does not interact with surfaces when freely swimming through the middle plane). BV trajectories were recorded on the surface of the coverslip (*B*), the middle plane (*C*), and slide (*D*) (a sum of 290, 296, and 305 trajectories drawn from four samples, respectively). The signed curvature (helicity) histograms on the coverslip (*E*), middle plane (*F*), and slide (*G*) show a transition from counterclockwise to clockwise rotations. Positive curvature values indicate clockwise rotation, while negative curvature values indicate counterclockwise rotation. The helicity data are summarized in (*H*) by approximating trajectories as circles with the radius R_{eff} of $2/(\kappa_{\text{ave}} + \kappa_{\text{median}})$, where κ_{ave} and κ_{median} are the mean and median for the corresponding curvature histogram (see the Supporting Material for details of the calculation). The helicity of the circles on the surfaces depend on the bacterium's distance from the surface, the bacterium's shape, its propulsion mechanism, and the size and shape of the bacterium (29) (see the Supporting Material for detailed discussion). In addition, there are differences in the surface roughnesses that are reflected as slight differences in how bacteria interact with the coverslip and the microscope slide surface. These differences arise, for instance, because the coverslip has more debris while dead bacteria tend to stick to the slide. In (*I*), we show histograms of speed as well as duration and lengths of trajectories on each plane shown for those trajectories given in (*B*)–(*D*). Frequency in all plots represents trajectory count. (*J*) Hydrodynamic simulations from Spagnolie and Lauga (29)—adapted to match our boundary conditions—demonstrate that hydrodynamic interactions are sufficient to account for switching helicity (and trajectory radius size changes) as bacteria move between two surfaces with a z-range set arbitrarily between 1 and 3. BV dwell longer at the coverslip and microscope slide (0 being the coverslip plane), indicating that mobile BV is hydrodynamically forced onto surfaces (*K*). Each data point here represents the average dwell time of 20 trajectories recorded at that specific plane. Tracking criteria are explained in Materials and Methods. The helicity of all trajectories in figures in the main body and Supporting Material are opposite to the observations as seen in the movies (in other words, as seen from the coverslip side of our inverted setup). To see this figure in color, go online.

above suggest—in agreement with other recent studies on bacteria, e.g., Sipos et al. (30) and Berke et al. (31)—that hydrodynamic interactions dominate BV's behavior and dictate its accumulation on surfaces.

Next, we surmised that if the components of the hydrodynamic force induced by the swimming of BV perpendicular to the surface, along which BV swims, were important, then we should see BV preferentially swim along walls (30,35). Sample trajectories showing BV preferentially swimming along walls are shown in Fig. 3 with more data in Fig. S5.

Extending this logic to solid (chemically inert) beads as walls of finite radii, we should expect BV to be "geometrically captured" (25) in orbits around beads resting on the coverslip, with the dwell time of BV around the bead increasing with the bead's radius when capture is successful. This behavior, not yet observed to our knowledge in living organisms, would be consistent with the behavior of previously reported inanimate self-propelled Au-Pt particles (1, 2, and 4 μm) suspended in hydrogen peroxide solution captured in orbits closely following solid spheres (diameter 1–125 μm) (25).

To determine whether BV is geometrically captured, we explored mobile BV's behavior in the presence of inert (i.e., chemoattractant-free) and electrically neutral CL beads; see Materials and Methods and Fig. 3. We sandwiched active BV and CL beads—within a range of radii 20–60 μm—between a microscope slide and a coverslip (with sealed edges; see Fig. 3 *A*). Our results reveal that mobile BV orbits around beads (here of radius 56 μm) (Fig. 3 *C*; Movie S4), and shows a higher population density around them (Figs. 3 *D*, S6, and S7) by virtue of the same hydrodynamic forces that made BV swim along walls (Fig. 3 *B*) and generated higher densities of mobile BV near flat surfaces (Fig. 2). BV's density dramatically drops off to a background level within a few BV body lengths from the bead surface (~4–5 μm in

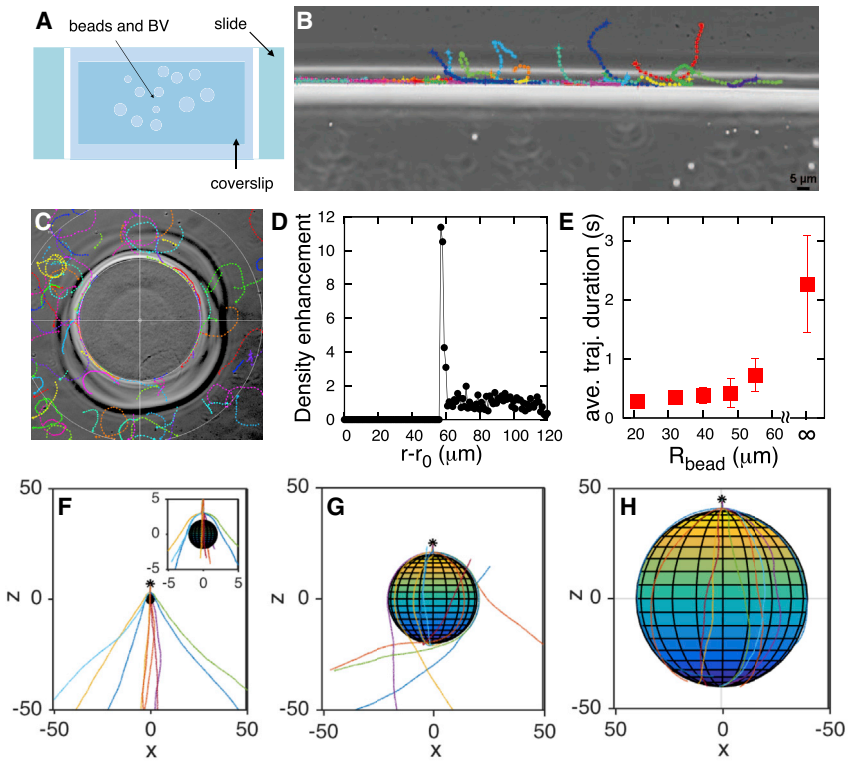

FIGURE 3 BV is geometrically captured in orbital motion around spherical inert beads. Active BV are mixed with inert CL beads between a microscope slide and a coverslip (*A*). Sample trajectories show BV swimming along a wall (constructed as explained in the Materials and Methods) (*B*), and being geometrically captured around beads (*C*). Each colored line indicates a separate bacterial trajectory, with the points along each line indicating the position of the bacterium at each interval. From 84 trajectories, we collected a density histogram (see the Supporting Material for details of the calculation) of BV showing how BV tightly localizes in orbital motion around beads (*D*). Density enhancement is computed with respect to the center of the bead (r_0) as explained in the Supporting Material and Fig. S7. Analysis of beads of decreasing size reveal how BV's capture time decreases for smaller beads (*E*). Each data point is the mean trajectory's duration within the capture region (5 μm from the bead surface) for a corresponding bead after dropping 5% of outliers from each side (that is, bacteria that stayed stuck to the bead or bacteria that only grazed the bead). The error bar is 1 SD. The data point corresponding to $R_{bead} = \infty$ shows the trajectory duration expected for an infinite radius bead (obtained by averaging the trajectory duration on the surface of the coverslip and slide combined; from Fig. 2, *B* and *D*). More data are provided in Figs. S6 and S7. Simulations of BV trajectories are shown around beads with radii of 2 (*F*), 20 (*G*), and 40 (*H*), measured in units of BV's bacterial body length with identical initial conditions. Model details are found in the Fig. S2 and the Supporting Material. The capture probability increases (from ~0 to ~1) as the bead size increases from 2 (*F*) to 40 (*H*). Strong interactions with the surface on which the bead rests contribute to BV's eventual detachment from the bead in experiments. To see this figure in color, go online.

Fig. 3 *D*). This means that beyond this typical distance, BV does not hydrodynamically interact with surfaces. This is in agreement with previous findings on self-generated bacterial flow field profiles for *E. coli*, which demonstrated that the flow field dissipates within a few bacterial body lengths from the cell (20).

Next, we eliminated the possibility that BV hunts by being geometrically captured by its prey. Experiments (Fig. 3 *E*) and simulations (Fig. 3, *F–H*, using a model adapted from Spagnolie et al. (36)) reveal that as we reduce the bead size ($\leq$40 μm), hydrodynamic forces no longer successfully capture BV. Furthermore, theory predicts (see Fig. S2 and the Supporting Material for details) that grazing trajectories become increasingly less curved as the size of the bead is reduced.

Because BV cells have electrically charged membranes, we assured ourselves that successful capture by larger beads is due to hydrodynamics and not possible residual electric charge on the beads we were using by monitoring BV's geometric capture around both positively charged (DEAE Sepharose Fast Flow) and negatively charged (SP Sepharose Fast Flow) beads (see details in Fig. S8). While BV is attracted to and eventually sticks to positive beads (therefore BV's surface is negatively charged), it still orbits around negatively charged beads, albeit more weakly, indicating that hydrodynamic interactions can even overcome weak electrostatic repulsion.

While BV is not successfully geometrically captured by objects as small as its bacterial prey, geometric capture by BV is a generic phenomenon that depends on: 1) the presence of an approximate no-slip boundary; and 2) the fact that BV's body rotates and thereby perturbs its liquid environment. We therefore hypothesize that its prey must also be susceptible to its own self-generated hydrodynamic fields and that these effects may passively colocalize predator and prey to improve the probability of chance collisions between BV and its prey. Thus, we repeated all experiments (on surfaces, along the wall, and around beads) with *E. coli*, a natural Gram-negative prey for BV (3). We found that *E. coli* also shows circling trajectories with opposite helicities on the coverslip and slide (Fig. 4 *A*), thereby confirming that *E. coli* is also influenced by its own self-induced hydrodynamic forces, consistent with Frymier et al. (23) and Lauga et al. (24). Fig. 4 recapitulates all the results for *E. coli* that were found for BV with walls and beads (Movie S5). In particular, we observed an enhancement of mobile density near solid objects, indicating geometric capture, and a density decrease 5–7 μm away from the bead's surface (compare with Fig. 3 for BV). We also repeated our controls with charged beads (with similar results) for *E. coli* (see Fig. S9).

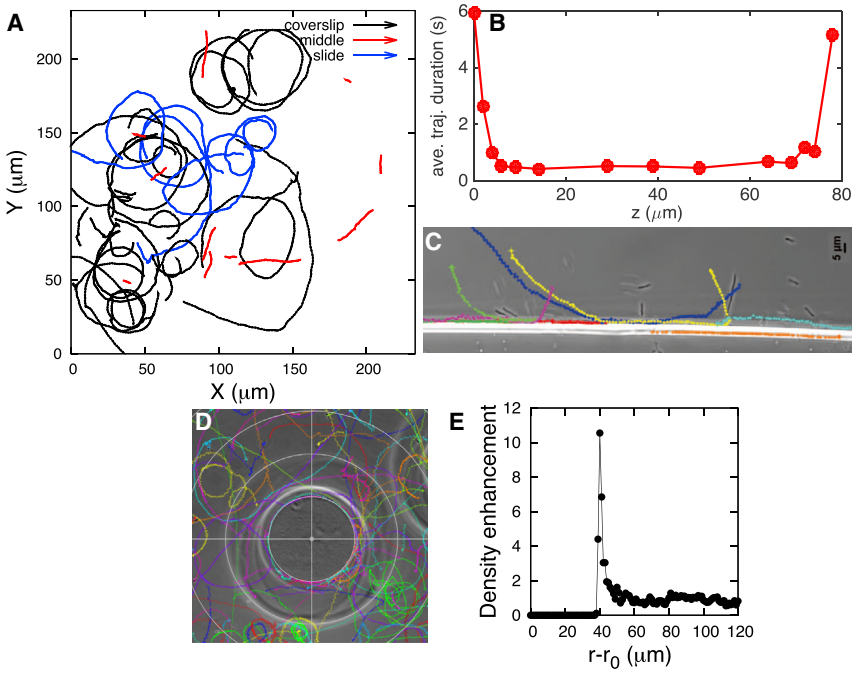

FIGURE 4 *E. coli* is also influenced by its own self-generated hydrodynamic fields. Like BV, *E. coli* circles on the coverslip and slide with opposite helicity (*A*), and sticks closely to surfaces and the wall (constructed as explained in Materials and Methods) (*B* and *C*). Based on a total of 24 trajectories of *E. coli* on the surfaces, we calculated a radius that was approximately twice as large as that of BV. This is expected from our hydrodynamic model as *E. coli* is longer than BV; based on our hydrodynamic model, longer bacteria make bigger circles on the surfaces (see the Supporting Material for detailed discussion). (*B*) Dwell time for trajectories recorded on each plane between a coverslip and a microscope slide, 0 being the coverslip plane. Like BV, *E. coli* is also geometrically captured by beads (*D*) (trajectories are recorded on the surface of the coverslip around the bead). Just as determined in Fig. 3 *D* for BV, mobile *E. coli* spends more time around the bead, showing enhanced density near the bead by contrast to regions away from the bead as seen in (*E*) (86 trajectories). To see this figure in color, go online.

We should point out that the large density of BV around the cluster of *E. coli* (Fig. 1 *D*) is not due to hydrodynamic forces. The cluster of *E. coli* that is used in this experiment is ~10 μm—much smaller than beads that successfully capture BV. Indeed, based on Fig. 3 *E* (experimental results) and Fig. S2 *B* (simulation results), the capture time for BV by a bead of radius 10 μm is negligible.

Our results thus show that hydrodynamic forces confine both predator and prey to surfaces (two-dimensional, 2D) and around defects on the surfaces such as small beads (one-dimensional, 1D), and we hypothesize that this in turn may increase the rate of random encounters between the predator and its prey. Fig. 5 shows the outcome of simulation for the encounter rates of the predator with the prey expected from our experimental results. Indeed, encounter times (times between two successive collisions) decrease dramatically from bulk solution (three-dimensional, 3D) to the surfaces (2D), and to the boundaries around the defects on the surfaces (1D). Furthermore, when considering the surface accumulation of the BV and *E. coli* near surfaces and along the defects (density enhancement due to hydrodynamic interactions), the decrease in the encounter time from 3D to 1D is even more pronounced (Fig. 5 *B*, *red circles* versus *black squares*). The overall effect is a reduction in encounter times between BV and *E. coli* especially pronounced at low densities (such as 0.125×10^6 pairs per mL; that is, one pair in (200 μm^3)) from hours to seconds. BV's life cycle includes an attack phase followed by a growth phase totaling 3–4 h (15). By contrast, *E. coli* has a much shorter life cycle (~0.5 h). Thus, while an encounter may make the difference between a successful and unsuccessful hunt for BV, it is only a drop in the bucket for the much more rapidly dividing *E. coli*. We hypothesize that this may be why BV has evolved to move quickly as its velocity makes it more susceptible to being affected by its own hydrodynamic forces.

CONCLUSIONS

While BV may be useful in targeting encapsulated prey that can otherwise resist eradication efforts (37), and may even serve as a living antibiotic by reducing bacterial infections in livestock (5), poultry (9), and possibly humans (38), the most basic features of BV's hunting strategy have remained elusive (15). In addition, BV has recently successfully been used in vivo in antibacterial therapy, suggesting this predatory bacterium as a promising candidate to fight antibiotic-resistant bacteria that present a serious rising concern (39). BV could have sought active prey by detecting chemotactic signals. However, because both predator and prey are active, not only would the predator have required high sensitivity to detect single prey but it may also have required the predator to forecast its prey's future position based on available information. Instead, our results provide, to our knowledge, a new perspective on bacterial predation that may explain why previous chemotactic studies of BV for its prey were inconclusive: Mobile BV use passive hydrodynamic forces to reduce their search space for prey from an undirected 3D search to an equally undirected search either confined to a surface or to a 1D motion around a large enough defect, thereby dramatically improving BV's odds of a chance

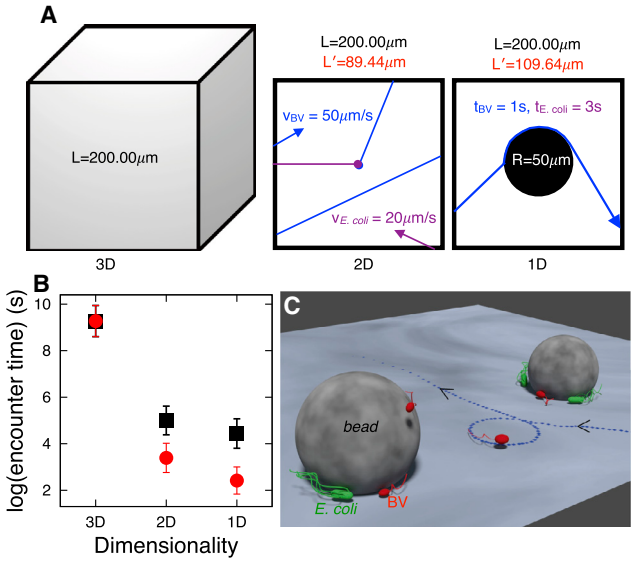

FIGURE 5 Hydrodynamic interactions, passively, enhance encounter rates of the predator with the prey. (*A*) Here we illustrate how we calculate the encounter rates of the predator with the prey using our experimental results. A cube of length $L = 200.00$ μm is considered to simulate encounter rates in 3D (*left*), the area of a square of the same length for 2D (*center*), and to capture the motion along the boundary of the beads on the surface of the coverslip, a circle of radius $R = 50$ μm inside the same square for 1D (*right*). A pair of BV and *E. coli*—with radii $r_{BV} = 0.50$ μm and $r_{E.coli} = 1.00$ μm (approximated as *spheres*)—initially start at the center of the cube and square and select a random direction, then move in straight paths with speeds of $v_{BV} = 50.00$ μm/s and $v_{E.coli} = 20.00$ μm/s (from experimental data, Fig. 2 *I*), respectively. When any of them collide with the surface of the cube (3D) or edge of the square (2D and 1D), they start from a new random position with a new random direction on a new random side of the cube or square (all uniformly). In the 1D case, they initially start from an arbitrarily point outside of the circle, and when they encounter the circle, they move along its circumference—BV for 1.0 s (Fig. 3 *E*) and *E. coli* for 3.0 s (averaged from 10 trajectories of *E. coli* along the bead surface on the coverslip) and then escape in a direction tangential to the circle. We record their positions at every 0.020 s (corresponding to a frame rate of 50 fps), and we consider a frame as an encounter time whenever the distance between BV and *E. coli* centers is less than $r_{BV} + r_{E.coli}$. We calculate encounter times from 1000 such collisions. (*B*) Natural logarithm of the encounter times (times between two successive encounters). (*Black squares*) Encounter times versus dimensionality without considering density enhancement (due to hydrodynamic effects); (*red circles*) corresponding times in the presence of the density enhancement. For red circles in 2D and 1D, we enhance the density fivefold to mimic density increases at surfaces due to hydrodynamics (Figs. 2 *K* and 4 *B*). We do so by reducing the length of the box from $L = 200.00$ μm to $L' = 89.44$ μm (2D) and to $L' = 109.64$ μm (1D). Error bars in (*B*) are 1 SD. (*C*) A qualitative illustration of geometric capture of predator and prey on surfaces and around beads as a result of their hydrodynamic interactions. To see this figure in color, go online.

collision. How these hydrodynamic effects could manifest themselves in vivo (39) as well as BV's natural habitat are the subject of future investigations. Our work may provide a starting point to investigate hydrodynamic effects on bacterial interactions that go beyond the chemical-sensing paradigm.

SUPPORTING MATERIAL

Supporting Materials and Methods, nine figures, and five movies are available at http://www.biophysj.org/biophysj/supplemental/S0006-3495(17)30218-7.

AUTHOR CONTRIBUTIONS

S. Pressé supervised all research and directed the theory; S. Pressé and G.G.A. codirected experiments; H.J., M.A.J., and N.M. performed all experiments; T.N., B.M., V.M., S. Perkins, and R.W. assisted in most experiments; B.D.R. provided technical support for experiments; H.J., C.W., K.T., and S. Pressé developed the theory; H.J., G.G.A., and S. Pressé wrote the article; and all authors participated in editing the article.

ACKNOWLEDGMENTS

S. Pressé acknowledges the National Science Foundation (NSF under grant No. MCB 1412259); G.G.A. acknowledges the National Institutes of Health (NIH under grant No. 1R03AR068724-01); and H.J. acknowledges a Graduate Student Imaging Research Fellowship from the Indiana University - Purdue University Indianapolis (IUPUI) Office of the Vice Chancellor for Research.

SUPPORTING CITATIONS

References (40–42) appear in the Supporting Material.

REFERENCES

1. Stolp, H., and M. P. Starr. 1963. *Bdellovibrio bacteriovorus* gen. et sp. n., a predatory, ectoparasitic, and bacteriolytic microorganism. *Antonie van Leeuwenhoek.* 29:217–248.
2. Rendulic, S., P. Jagtap, …, S. C. Schuster. 2004. A predator unmasked: life cycle of *Bdellovibrio bacteriovorus* from a genomic perspective. *Science.* 303:689–692.
3. Straley, S. C., and S. F. Conti. 1977. Chemotaxis by *Bdellovibrio bacteriovorus* toward prey. *J. Bacteriol.* 132:628–640.
4. Kadouri, D., and G. A. O'Toole. 2005. Susceptibility of biofilms to *Bdellovibrio bacteriovorus* attack. *Appl. Environ. Microbiol.* 71:4044–4051.
5. Boileau, M. J., K. D. Clinkenbeard, and J. J. Iandolo. 2011. Assessment of *Bdellovibrio bacteriovorus* 109J killing of *Moraxella bovis* in an in vitro model of infectious bovine keratoconjunctivitis. *Can. J. Vet. Res.* 75:285–291.
6. Lambert, C., I. T. Cadby, …, A. L. Lovering. 2015. Ankyrin-mediated self-protection during cell invasion by the bacterial predator *Bdellovibrio bacteriovorus*. *Nat. Commun.* 6:8884.
7. Rogosky, A. M., P. L. Moak, and E. A. Emmert. 2006. Differential predation by *Bdellovibrio bacteriovorus* 109J. *Curr. Microbiol.* 52:81–85.
8. Dashiff, A., R. A. Junka, …, D. E. Kadouri. 2011. Predation of human pathogens by the predatory bacteria *Micavibrio aeruginosavorus* and *Bdellovibrio bacteriovorus*. *J. Appl. Microbiol.* 110:431–444.
9. Atterbury, R. J., L. Hobley, …, R. E. Sockett. 2011. Effects of orally administered *Bdellovibrio bacteriovorus* on the well-being and *Salmonella* colonization of young chicks. *Appl. Environ. Microbiol.* 77:5794–5803.
10. Shatzkes, K., R. Chae, …, D. E. Kadouri. 2015. Examining the safety of respiratory and intravenous inoculation of *Bdellovibrio bacteriovorus* and *Micavibrio aeruginosavorus* in a mouse model. *Sci. Rep.* 5:12899.
11. Hobley, L., R. K. Fung, …, R. E. Sockett. 2012. Discrete cyclic di-GMP-dependent control of bacterial predation versus axenic growth in *Bdellovibrio bacteriovorus*. *PLoS Pathog.* 8:e1002493.

12. Rotem, O., J. Nesper, …, E. Jurkevitch. 2015. An extended cyclic di-GMP network in the predatory bacterium *Bdellovibrio bacteriovorus*. *J. Bacteriol.* 198:127–137.
13. Lambert, C., M. C. M. Smith, and R. E. Sockett. 2003. A novel assay to monitor predator-prey interactions for *Bdellovibrio bacteriovorus* 109 J reveals a role for methyl-accepting chemotaxis proteins in predation. *Environ. Microbiol.* 5:127–132.
14. Varon, M., and B. P. Zeigler. 1978. Bacterial predator-prey interaction at low prey density. *Appl. Environ. Microbiol.* 36:11–17.
15. Lambert, C., K. A. Morehouse, …, R. E. Sockett. 2006. *Bdellovibrio:* growth and development during the predatory cycle. *Curr. Opin. Microbiol.* 9:639–644.
16. Varon, M., and M. Shil. 1968. Interaction of *Bdellovibrio bacteriovorus* and host bacteria. I. Kinetic studies of attachment and invasion of *Escherichia coli* B by *Bdellovibrio bacteriovorus*. *J. Bacteriol.* 95:744–753.
17. Bray, D., M. D. Levin, and K. Lipkow. 2007. The chemotactic behavior of computer-based surrogate bacteria. *Curr. Biol.* 17:12–19.
18. Jashnsaz, H., T. Nguyen, …, S. Pressé. 2015. Inferring models of bacterial dynamics toward point sources. *PLoS One.* 10:e0140428.
19. Lauga, E. 2016. Bacterial hydrodynamics. *Annu. Rev. Fluid Mech.* 48:105–130.
20. Drescher, K., J. Dunkel, …, R. E. Goldstein. 2011. Fluid dynamics and noise in bacterial cell-cell and cell-surface scattering. *Proc. Natl. Acad. Sci. USA.* 108:10940–10945.
21. Kaya, T., and H. Koser. 2012. Direct upstream motility in *Escherichia coli*. *Biophys. J.* 102:1514–1523.
22. Hu, J., A. Wysocki, …, G. Gompper. 2015. Physical sensing of surface properties by microswimmers—directing bacterial motion via wall slip. *Sci. Rep.* 5:9586.
23. Frymier, P. D., R. M. Ford, …, P. T. Cummings. 1995. Three-dimensional tracking of motile bacteria near a solid planar surface. *Proc. Natl. Acad. Sci. USA.* 92:6195–6199.
24. Lauga, E., W. R. DiLuzio, …, H. A. Stone. 2006. Swimming in circles: motion of bacteria near solid boundaries. *Biophys. J.* 90:400–412.
25. Takagi, D., J. Palacci, …, J. Zhang. 2014. Hydrodynamic capture of microswimmers into sphere-bound orbits. *Soft Matter.* 10:1784–1789.
26. Kuchma, S. L., J. P. Connolly, and G. A. O'Toole. 2005. A three-component regulatory system regulates biofilm maturation and type III secretion in *Pseudomonas aeruginosa*. *J. Bacteriol.* 187:1441–1454.
27. Blattner, F. R., G. Plunkett, 3rd, …, Y. Shao. 1997. The complete genome sequence of *Escherichia coli* K-12. *Science.* 277:1453–1462.
28. Taktikos, J., V. Zaburdaev, and H. Stark. 2011. Modeling a self-propelled autochemotactic walker. *Phys. Rev. E Stat. Nonlin. Soft Matter Phys.* 84:041924.
29. Spagnolie, S. E., and E. Lauga. 2003. Hydrodynamics of self-propulsion near a boundary: predictions and accuracy of far-field approximations. *J. Fluid Mech.* 700:105–147.
30. Sipos, O., K. Nagy, …, P. Galajda. 2015. Hydrodynamic trapping of swimming bacteria by convex walls. *Phys. Rev. Lett.* 114:258104.
31. Berke, A. P., L. Turner, …, E. Lauga. 2008. Hydrodynamic attraction of swimming microorganisms by surfaces. *Phys. Rev. Lett.* 101:038102.
32. Li, G., and J. X. Tang. 2009. Accumulation of microswimmers near a surface mediated by collision and rotational Brownian motion. *Phys. Rev. Lett.* 103:078101.
33. Lee, C. F. 2013. Active particles under confinement: aggregation at the wall and gradient formation inside a channel. *New J. Phys.* 15:055007.
34. Elgeti, J., and G. Gompper. 2013. Wall accumulation of self-propelled spheres. *Europhys. Lett.* 101:48003.
35. Yazdi, S., A. M. Ardekani, and A. Borhan. 2015. Swimming dynamics near a wall in a weakly elastic fluid. *J. Nonlinear Sci.* 25:1153–1167.
36. Spagnolie, S. E., G. R. Moreno-Flores, …, E. Lauga. 2015. Geometric capture and escape of a microswimmer colliding with an obstacle. *Soft Matter.* 11:3396–3411.
37. Koval, S. F., and M. E. Bayer. 1997. Bacterial capsules: no barrier against *Bdellovibrio*. *Microbiology.* 143:749–753.
38. Sockett, R. E., and C. Lambert. 2004. *Bdellovibrio* as therapeutic agents: a predatory renaissance? *Nat. Rev. Microbiol.* 2:669–675.
39. Willis, A. R., C. Moore, …, R. E. Sockett. 2016. Injections of predatory bacteria work alongside host immune cells to treat Shigella infection in Zebrafish Larvae. *Curr. Biol.* 26:3343–3351.
40. Gabel, C. V., and H. C. Berg. 2003. The speed of the flagellar rotary motor of *Escherichia coli* varies linearly with protonmotive force. *Proc. Natl. Acad. Sci. USA.* 100:8748–8751.
41. Qian, C., C. C. Wong, …, K.-H. Chiam. 2013. Bacterial tethering analysis reveals a "run-reverse-turn" mechanism for *Pseudomonas* species motility. *Appl. Environ. Microbiol.* 79:4734–4743.
42. Swindells, J. F., C. F. Snyder, …, P. E. Golden. 1958. Viscosities of Sucrose Solutions at Various Temperatures: Tables of Recalculated Values. Supplement to National Bureau of Standards Circular, Vol. 440. National Bureau of Standards, Gaithersburg, MD, pp. 1–7.

Biophysical Journal, Volume *112*

Supplemental Information

Hydrodynamic Hunters

Hossein Jashnsaz, Mohammed Al Juboori, Corey Weistuch, Nicholas Miller, Tyler Nguyen, Viktoria Meyerhoff, Bryan McCoy, Stephanie Perkins, Ross Wallgren, Bruce D. Ray, Konstantinos Tsekouras, Gregory G. Anderson, and Steve Pressé

Supporting Material

Hydrodynamic Hunters

Hossein Jashnsaz, Mohammed Al Juboori, Corey Weistuch, Nicholas Miller†, Tyler Nguyen†, Viktoria Meyerhoff‡, Bryan McCoy‡, Stephanie Perkins‡, Ross Wallgren‡, Bruce D. Ray, Konstantinos Tsekouras, Gregory G. Anderson *, Steve Pressé *

∗ **Corresponding authors. Email: stevenpresse@gmail.com (S.P.); ga2@iupui.edu (G.G.A)**

† These authors contributed equally to this work.

‡ These authors contributed equally to this work.

Supporting Material Methods

I. Algorithm to calculate the "signed curvature" (helicity)

We consider three adjacent points on a trajectory (i^{th} trajectory) in a 2D Cartesian coordinate system as $\mathbf{r_{j-1}}(x_{j-1}, y_{j-1})$, $\mathbf{r_j}(x_j, y_j)$, and $\mathbf{r_{j+1}}(x_{j+1}, y_{j+1})$ (Fig. S1A). Throughout this calculation, we use i as the trajectory index, and j as the point (frame) index on a specific trajectory. At the middle point, the absolute value of the curvature, designated by $\varkappa_j$, is

$$\varkappa_j = \frac{|c_j|}{[1 + (dy/dx|_j)^2]^{3/2}}. \tag{1}$$

where

$$c_j = \frac{d^2y}{dx^2}|_j = \frac{m_{1j} - m_{2j}}{(x_{j+1} - x_{j-1})/2}, \tag{2}$$

$$m_{1j} = \frac{y_j - y_{j-1}}{(x_j - x_{j-1})}, \tag{3}$$

$$m_{2j} = \frac{y_{j+1} - y_j}{(x_{j+1} - x_j)}, \tag{4}$$

$$\frac{dy}{dx}|_j = \frac{m_{1j} + m_{2j}}{2}. \tag{5}$$

We define the sign, φ_j, for the curvature as follows

$$\varphi_j = \frac{y_j - y_M}{|y_j - y_M|} \frac{x_{j+1} - x_{j-1}}{|x_{j+1} - x_{j-1}|} = \begin{cases} +1 & \text{for } cw, \\ -1 & \text{for } ccw, \end{cases} \tag{6}$$

where cw is for clockwise and ccw is for counterclockwise and where

$$y_M = y_{j-1} + (x_{j+1} - x_j) \frac{y_{j+1} - y_{j-1}}{(x_{j+1} - x_{j-1})}. \tag{7}$$

Now we define the signed curvature or helicity as:

$$\kappa_j = \varphi_j \varkappa_j. \tag{8}$$

We repeat the same calculation for all points (excluding the first and the last point) along the i^{th} trajectory then find the average curvature for this trajectory using $\bar{\kappa_i} = \frac{1}{M_i - 2} \sum_{j=2}^{M_i - 1} \kappa_j$, where M_i is the number of points (frames) along the i^{th} trajectory. We define the effective radius for the i^{th} trajectory as $R_i = 1/\bar{\kappa_i}$. Then we find the mean curvature and mean effective radius of N such trajectories ($\bar{\kappa} = \frac{1}{N} \sum_{i=1}^{N} \kappa_i$, $\bar{R} = \frac{1}{N} \sum_{i=1}^{N} R_i$). Negative values of R_i or $\bar{R}$ represent a ccw rotational direction. As an example, we apply this algorithm on synthetic ccw and cw circular trajectories in Fig. S1.

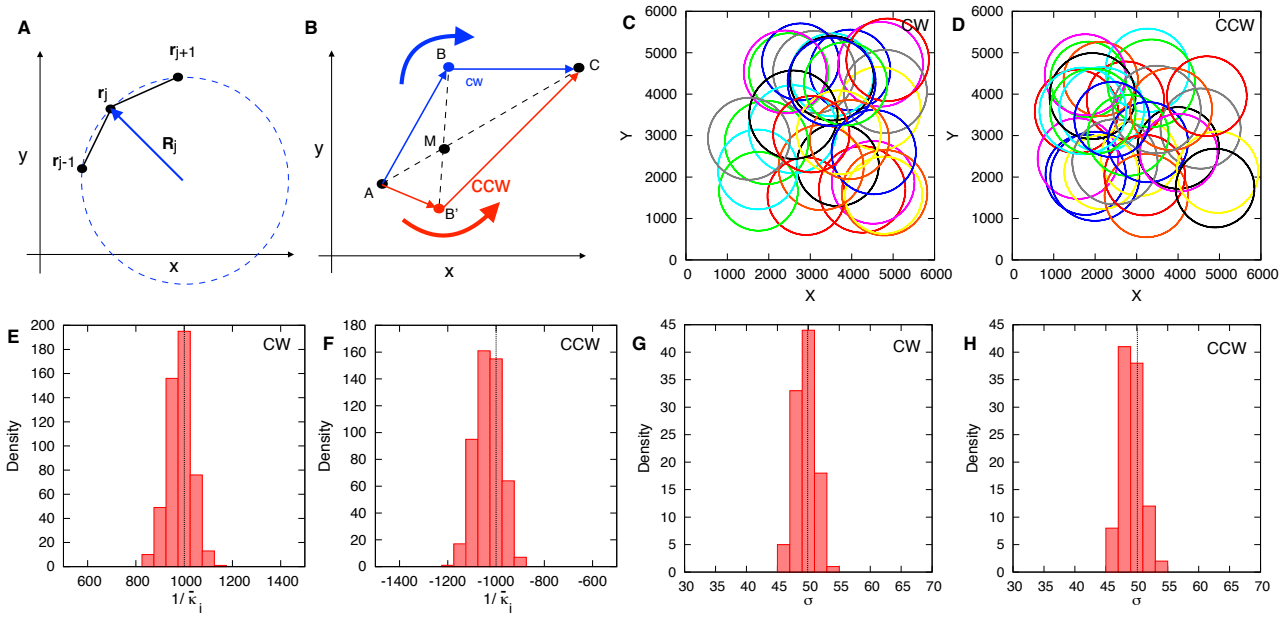

FIGURE S1. Illustration of our algorithm for computing signed curvatures (helicities). (A) We calculate the curvature by having 3 data points (curvature around midpoint) using Eq. 1 in Supplementary Text, and the radius of a circle – going through all 3 points – is approximated by this curvature in the limit that step sizes are much smaller than the radius. (B) We quantitively define a "signed curvature" (helicity) as follows: We consider the following data points: $A(x_{j-1}, y_{j-1}), C(x_{j+1}, y_{j+1}), M(x_M, y_M)$, $B(x_j, y_j)$, and $B'(x_j, y_j)$. ABC represents a cw helicity while $AB'C$ represents a ccw helicity. In this specific case, if $y_j > y_M$ the curve is cw, for $y_j < y_M$ the curve is ccw, and for $y_j = y_M$ it would be a straight line. M is the intersection of a line parallel to the y-axis from B (or equivalently from B' for ccw curve) and AC. This is how we use Eq. 6 and Eq. 7 in Supplementary Text, to define the sign of the curvature for the most general case. In order to test this algorithm, we generated cw and ccw (circular) trajectories. We show sample cw (C) and ccw (D) trajectories. The center for the circle i (or i^{th} trajectory), (x_i^c, y_i^c), is sampled from a uniform distribution $(1500 < x_i^c \& y_i^c < 5000)$ and its radius (R_i) is sampled from a normal distribution $(R_i \sim N(\mu_R, \sigma_R)$ with $\mu_R = 1000$ and $\sigma_R = 50$, shown with vertical dotted lines on the histograms. $x_{ji} = x_i^c + R_i \cos(\theta_j)$ and $y_{ji} = y_i^c + R_i \sin(\theta_j)$ are the coordinates of the j^{th} point on the i^{th} circle. θ_j goes from 0 to 2π for a ccw circle, while it goes from 2π to 0 for a cw circle, both with uniform steps of $2\pi/360$. We use our algorithm to calculate μ_R and σ_R from the generated data. We show histograms of inverse average curvatures for 500 circular cw (E) and ccw (F) trajectories. The dashed vertical lines show the theoretical values of μ_R. We show histograms of the standard deviation of the inverse average curvature for cw (G) and ccw (H) trajectories. The dashed vertical lines show the theoretical values of σ_R.

II. Density calculation

Density profiles shown in Figs. 3 and 4, and Figs. S4 and S7 are calculated as follows: concentric circular rings – of radius r_i – are considered around the center of the beads. The density at r_i is calculated according to $n_i = N_i/dA_i$, where N_i is the number of frames (points) within the area between r_i and r_{i+1}, and $dA_i = A_{i+1} - A_i$ where A_i is πr_i^2. Background densities are calculated with respect to points

away from the bead center. Density enhancements are calculated as the density with respect to the bead center divided by the average background density at various distances from the bead center. All densities are taken from motile bacteria only.

III. Modeling hydrodynamic interactions of BV with surfaces and spherical objects

To simulate BV's behavior between two opposing surfaces, we adapted a model presented in Ref. 1. We considered the surfaces far enough apart that the effect of one surface doesn't effect the other surface. In addition, we implemented a model from Ref. 2 to simulate BV's interaction with spherical beads.

We briefly summarize key parts of both models here – with equations superscripted s for BV's interaction with surfaces, and equations superscripted b for BV's interaction with beads – from Refs. 1, 2. The readers are referred to Refs. 1, 2 for additional details.

A far field hydrodynamic model is used in both cases. We modeled BV as a prolate spheroid, with a flagellum, in order to be able to use Faxén's laws (1). BV's dynamics can be modeled near a flat, no-slip surface using a linear combination of four hydrodynamic terms with Brownian fluctuations; to clarify, a no slip surface implies that the fluid velocity near the boundary approaches zero. The first of these terms, a force dipole, arises from the opposing directions of the flow field around the moving object. Higher order approximations lead to the other three terms: a force quadrupole term (due to the nonuniform flow fields around the body length), a source dipole (due to difference in hydrodynamic potential across the body), and a rotlet dipole (due to the opposing rotation of the body and the flagellum).

The rotlet dipole creates a rotation along an axis perpendicular to the surface (a qualitative effect observed in many bacteria near surfaces). The model also describes the orbiting of BV around beads. For this effect, only the force dipole term was considered, since BV must get much closer to a curved object for higher order terms to be necessary.

The actual terms are described using derivatives of a Green's function for the linearized Navier-Stokes equations (a stokeslet). This approximation is known to be valid for low Reynold's numbers.

We define two different coordinate systems: $\vec{r}_s$, $\vec{r}_s^{\perp}$ and $\vec{r}_b$,$\vec{r}_b^{\perp}$. Both $\vec{r}_s$ and $\vec{r}_b$ represent the components of the orientation vector $\vec{e}$ (BV's director) in the direction of the normal line connecting the surface and the BV and the normal line connecting the bead and the BV, respectively. To complete the decompositions, we consider the directions $\vec{r}_s^{\perp}$ and $\vec{r}_b^{\perp}$ as the remaining component of the orientation vector for each model, respectively (1, 2)

$$\vec{r_b} = \frac{\vec{x} - \vec{x}_b}{\|\vec{x} - \vec{x}_b\|} \tag{9}$$

$$\vec{r_b^{\perp}} = \frac{\vec{e} - (\vec{e} \cdot \vec{r}_b)\vec{r}_b}{\|\vec{e} - (\vec{e} \cdot \vec{r}_b)\vec{r}_b\|} \tag{10}$$

where $\vec{x}_b$ is the center of the spherical object. The terms for calculations near a surface were defined similarly.

The magnitude of the hydrodynamic forces on BV are proportional to the distance between BV's center of mass and the surface (or bead). We therefore define these distances as h_s and h_b respectively. The magnitude of the forces is related to BV's orientation angle with respect to each object. We therefore define the angle θ_s as

$$\theta_s = cos^{-1}\Big(\frac{\vec{v} \cdot \vec{r_s^{\perp}}}{\|\vec{v}\|\|\vec{r_s^{\perp}}\|}\Big). \tag{11}$$

θ_b is defined in the same way as above (2). If $(\vec{x} - \vec{x}_b) \cdot \vec{v} < 0$ we used $-\theta$ instead since the inverse cosine does not give a direction of the angle. $\vec{v}$ is BV's normalized natural velocity and is, therefore, equivalent to the orientation vector.

The dynamical equations for BV are then defined as:

$$d\vec{x}(t) = (\vec{v} + \vec{u})dt + \sqrt{6D}d\vec{B}_1(t) \tag{12}$$

$$d\vec{e}(t) = (\vec{\Omega}dt + \sqrt{4D_r}d\vec{B}_2(t)) \times \vec{e} \tag{13}$$

where $\vec{\Omega}$ is the hydrodynamic contribution to the torque, $\vec{u}$ is the hydrodynamic contribution to the velocity, and D and D_r are the translational and rotational diffusion constants, respectively. $\vec{B}_1(t)$ is a normal Brownian motion, while $\vec{B}_2(t)$ is a Brownian motion on a sphere. We assume that the bacterium does not directly contribute to the torque (which is observed in experiments).

The model is scaled according to the length of the body of the bacterium and the (assumed constant mean) velocity of the bacterium in free space. Time (t) is non-dimensionalized with respect to these two parameters (bacterium body length and its velocity). We assumed that the BV cannot be less than 1 of its radii away from a surface or bead (hard wall repulsion). The hydrodynamic contributions are, as

previously stated, a linear combination of terms such that:

$$\vec{u}^s = \vec{u}^s_{FD} + \vec{u}^s_{FQ} + \vec{u}^s_{SD} + \vec{u}^s_{RD} \tag{14}$$

$$\vec{u}^b = \vec{u}^b_{FD} \tag{15}$$

$$\vec{\Omega}^s = \vec{\Omega}^s_{FD} + \vec{\Omega}^s_{FQ} + \vec{\Omega}^s_{SD} + \vec{\Omega}^s_{RD} \tag{16}$$

$$\vec{\Omega}^b = \vec{\Omega}^b_{FD} \tag{17}$$

$$\vec{u}^s_{FD} = \frac{-3\alpha(1-3sin^2(\theta_s))}{8h_s^2}\vec{r}_s + \frac{3\alpha sin(2\theta_s)}{8h_s^2}\vec{r}_s^{\perp}; \text{(Eq. B6 in Ref. 1)} \tag{18}$$

$$\vec{u}^s_{FQ} = \frac{\beta sin(\theta_s)}{4h_s^3}(7-9sin^2(\theta_s))\vec{r}_s + \frac{\beta cos(\theta_s)}{16h_s^3}(7-27sin^2(\theta_s))\vec{r}_s^{\perp}; \text{(Eq. B9 in Ref. 1)} \tag{19}$$

$$\vec{u}^s_{SD} = \frac{-\zeta sin(\theta_s)}{h_s^3}\vec{r}_s + \frac{-\zeta cos(\theta_s)}{4h_s^3}\vec{r}_s^{\perp}; \text{(Eq. B14 in Ref. 1)} \tag{20}$$

$$\vec{u}^s_{RD} = 0; \text{(Eq. B17 in Ref. 1)} \tag{21}$$

$$\vec{u}^b_{FD} = \frac{-3A\delta(1-3sin^2(\theta_b))(A+h_b)}{2h_b^2(2A+h_b)^2}\vec{r}_b + \frac{3A^3\delta(2A^2+6Ah_b+3h_b^2)sin(2\theta_b)}{4h_b^2(A+h_b)^3(2A+h_b)^2}\vec{r}_b^{\perp}; \text{(Eq. 39 in Ref. 2)} \tag{22}$$

$$\vec{\Omega}^s_{FD} = \frac{-3\alpha sin(2\theta_s)}{16h_s^3}(1+\frac{\Gamma}{2}(1+sin^2(\theta_s))\vec{r}_s^{\perp}\times\vec{r}_s; \text{(Eq. B6 in Ref. 1)} \tag{23}$$

$$\vec{\Omega}^s_{FQ} = \frac{-3\beta cos(\theta_s)}{8h_s^4}(1-3sin^2(\theta_s)+\frac{\Gamma}{4}(11-3sin^4(\theta_s)))\vec{r}_s^{\perp}\times\vec{r}_s; \text{(Eq. B10 in Ref. 1)} \tag{24}$$

$$\vec{\Omega}^s_{SD} = \frac{3\zeta cos(\theta_s)}{8h_s^4}(1+\frac{3\Gamma}{2}(1+sin^2(\theta_s))\vec{r}_s^{\perp}\times\vec{r}_s; \text{(Eq. B14 in Ref. 1)} \tag{25}$$

$$\vec{\Omega}^s_{RD} = \frac{\nu cos(\theta_s)}{16h_s^3}(5-3\Gamma sin^2(\theta_s))\vec{r}_s + \frac{\nu sin(\theta_s)}{16h_s^3}(2+3\Gamma cos^2(\theta_s))\vec{r}_s^{\perp}; \text{(Eq. B17 in Ref. 1)} \tag{26}$$

$$\vec{\Omega}^b_{FD} = \frac{-3\delta A^3 sin(2\theta_b)}{4h_b^3(A+h_b)^2(2A+h_b)^3}\Big(2A^2+6Ah_b+3h_b^2-\frac{\Gamma Q}{8A^2(A+h_b)^2}\Big)\vec{r}_b^{\perp}\times\vec{r}_b; \text{(Eq. 40 in Ref. 2)} \tag{27}$$

$$Q = A^6 - 5A^4(A+h_b)^2 + 10A^2(A+h_b)^4 + 6(A+h_b)^6 + (9A^6 - 29A^4(A+h_b)^2 + 34A^2(A+h_b)^4 - 18(A+h_b)^6)cos(2\theta_b); \text{(Eq. 41 in Ref. 2)} \tag{28}$$

$$\Gamma = \frac{1-\gamma^2}{1+\gamma^2} \tag{29}$$

where γ is the aspect ratio (defined as the width divided by the length) of the bacterial body, α,β,ζ,ν, and δ (as dimensionless model parameters) are the strengths of the multipoles. FD, FQ, SD, and RD stand for force dipole, force quadrupole, source dipole, and rotlet dipole respectively. A is the radius of the spherical object. These terms are derived using the method of images (1, 2). The fluid flows under

the given boundary conditions can be constructed by placing identical swimmers behind the boundary. The image swimmers allow one to construct the unique flow field such that the boundary conditions are satisfied. These equations were simulated using a forward Euler algorithm. To prevent BV from moving through a wall, the component of BV's velocity in the direction of the wall was set to zero if a time step would move it beyond the wall.

Using a hydrodynamic model for BV's interaction with opposing surfaces, we have shown that our simulations are consistent with the experimental observation that bacteria rotate clockwise near the top of a coverslip (viewed from below; view direction being +z direction). The simulations show that BV switches its direction of rotation as it moves to the opposing surface, consistent with experimental observations. The radius of the circles depends on the distance to the surface, the strength of the rotlet dipole (which depends on the shape and propulsion mechanism of each individual bacterium), and the aspect ratio of the bacterium (Eq. 3.8 in Ref. 1). However, this is the relationship for a single surface. In our model, we looked at the motility of BV between two opposing surfaces, and thus the rotlet dipole is the sum of the rotlet dipoles from the top and bottom surface. In particular, assuming that the bacterium is parallel to the surfaces, we have a generalization of Eqs. 3.7 and 3.8 in Ref. 1 as follows:

$$z \cdot \Omega = -\frac{3\nu}{32h^4}(1-\Gamma) + \frac{3\nu}{32(h_{top}-h)^4}(1-\Gamma) \tag{30}$$

Therefore:

$$R_\tau = \frac{32}{3|\nu|(1-\Gamma)} \frac{(h(h_{top}-h))^4}{h^4-(h_{top}-h)^4}. \tag{31}$$

Clearly we see that this radius is infinite midway between the two planes (one surface being set to 0, and the other to h_{top}) no matter the parameters. This will always be where the direction of rotation changes and is consistent with our experimental and theoretical results. In addition, distance was nondimensionalized by the length of the semi-major axis of the bacterium.

Therefore, since *E.coli* has a much larger length than BV, it will generally swim in circles having a much larger radius. Furthermore, BV and *E. coli* have different rotlet dipole strengths as well as different aspect ratios. Although the effects of the last two factors are difficult to determine, it is expected that hydrodynamic effects would be stronger in BV than *E. coli* since BV generates larger hydrodynamic flows with respect to its body size and mass than *E. coli* resulting in the differences stated above.

In our model, the forces are scaled by the body length, free swimming velocity and viscosity. Therefore

in Eq. 30 we see that the radius will depend on viscosity, assuming that the dimensional angular velocity is fixed. For our experiments, this is expected to be the case. Therefore, we expect the swimming radius of our BV to increase with viscosity as observed in Fig. S4.

Furthermore, using a hydrodynamic model for BV's interaction with spherical beads, we show BV's capture probability vs bead radius increases. For a bead of $A = 2$ (roughly the size of *E. coli*), our model predicts there is no capture for BV. Our simulations show that *E. coli* is too small to capture a BV. The results of these simulations are shown in Fig. S2.

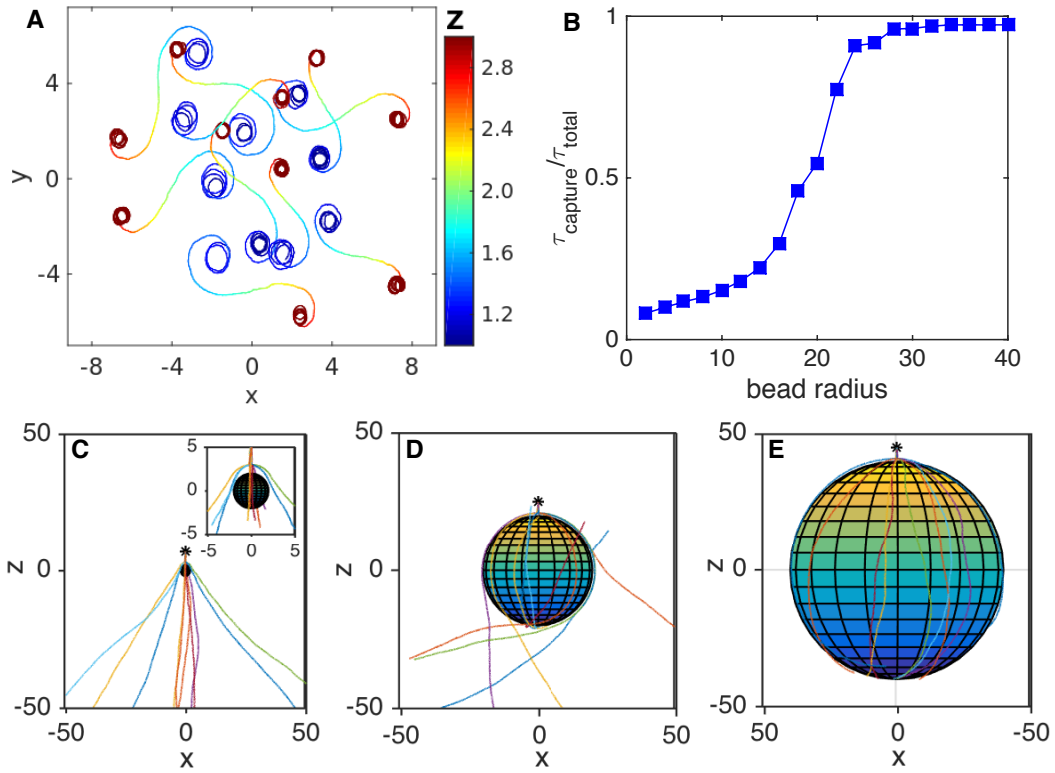

FIGURE S2. Our hydrodynamic model (given in Supplementary Text) predicts strong hydrodynamic interactions of BV with surfaces and spherical obstacles. (A) Here we show sample simulated trajectories of BV between two opposing surfaces. The color bar represents z. BV rotate in circular trajectories on the surfaces and show a rotational direction switch when moving from one surface to the other, with an increase in the curvature radius as it moves away from surfaces. The surfaces are set, arbitrarily, at $z = 0$ and $z = 4$. As for parameters (all dimensionless and defined in Supplementary Text), $D = 0.03$, $D_r = 0.75 \times D$, $\alpha = 0.8$, $\beta = -0.01$, $\zeta = 0.1$, $\nu = 12$, and $\gamma = 0.3$. All trajectories start with the same initial velocity, but with uniform random initial positions at $z = 1.01$ (within the shown xy range), and run from $t = 0$ to 30. To re-emphasize, equations with superscript s (given in Supplementary Text) are used for the part of simulation shown in this subplot. (B) BV's capture probability vs bead radius is shown as predicted by our hydrodynamic model for BV's interaction with spherical beads. Our metric compared the time the BV was circling the bead ($\tau_{capture}$) with the total simulation time (τ_{total}). As can be seen, BV is easily captured for larger beads, and the probability of capture goes to zero for beads the size of prey. In (C to E), reproduced for convenience, we show 10 sample trajectories of BV for $\delta = 0.8$ (the force dipole strength near the beads) around three instances of beads with radii of $A = 2$, 20, and 40, respectively, in units of the bacterial body length. All trajectories started at $(A+5, 0, 0)$, initially in -z direction, and ran from $t = 0$ to 120. The dimensionless diffusion coefficient is $D = 2.5 \times 10^{(-2)}$ here. To reemphasize, equations with superscript b (given in Supplementary Text) are used for the part of the simulation shown in (B to E). The probability of capture goes from 0 to 1 from (C) to (E). This capture probability is an upper bound. In real experiments, bacteria lose their orbit around beads by interacting with the neighboring surface on which the bead rests. The model excludes the possibility of interaction of bacteria with surfaces neighboring beads while on the bead (which reduces the bacterium's capture time). In addition, the model also excludes the possibility of collision of captured bacteria with debris, dead bacteria, and surface imperfections of the bead.

We have found no simple analytical expression relating the radius of the trajectories on the surface and the capture radius of a bead. In general, we can only say that the distance of the bacterium to the surface, the strength of the rotlet dipole and the aspect ratio of the bacterium contribute to the radius of the circular trajectory on the plane, while the bacterium's aspect ratio as well as the force dipole strength (Eq. 15 in Ref. 2) primarily contributes to the radius of the sphere above which there is effective capture.

BV's flagellar motor rotary state.

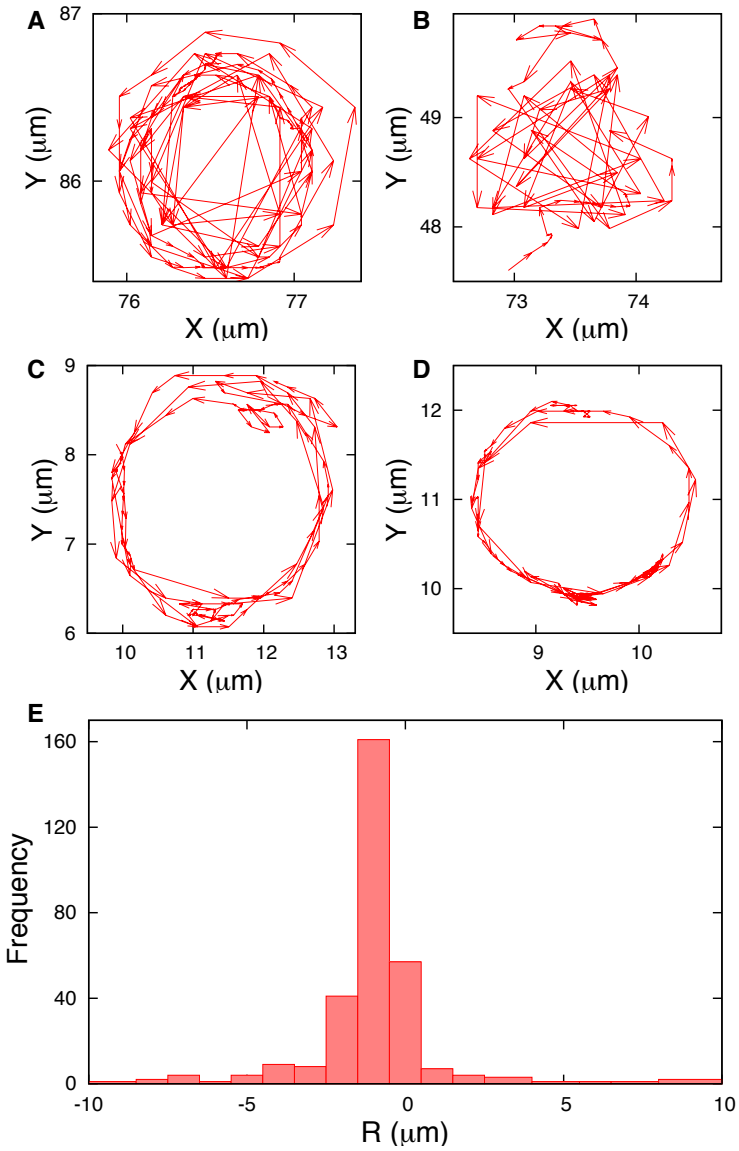

FIGURE S3. BV's flagellar motor rotates primarily in one direction (counterclockwise, ccw). BV's flagellum was tethered to coverslips (3) and their bodies' rotation recorded and analyzed (4). Here we show trajectories for four instances of BV's body rotation around the attachment point (at its flagellum) (A to D). A histogram for the effective radius (Supplementary Text) is given in (E). This analysis shows a strong bias in the rotation direction of the flagellum; the flagellum rotates effectively ccw when seen from its tip. Negative effective radius values (E) coincide with ccw rotations, while positive values coincide with clockwise (cw) rotations. Exclusively for this part of the experiments, we used BV strain 109J because its body is rather longer than strain 109, and this feature makes it possible to easily monitor its body's rotation.

Change in BV's trajectory curvature vs viscosity of the solution.

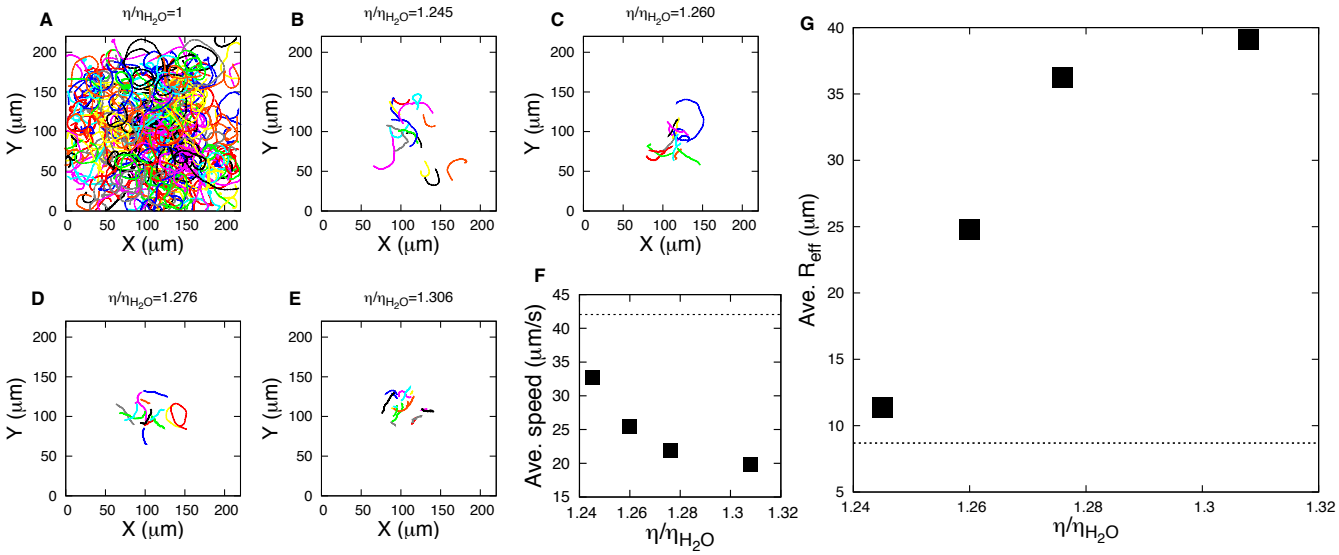

FIGURE S4. BV's trajectories straighten as the viscosity of the solution increases. Viscous solutions were prepared according to Tables 130 and 131 in Ref. 5, and BV trajectories were recorded on the coverslip. Here we show BV trajectories (A to E) from control ($\eta/\eta_{H_2O} = 1$) to highest viscosity. We show both BV's swimming speed (mean out of about 15 trajectories) vs viscosity (F), and the average effective radius of the trajectories vs viscosity (G). The dotted lines represent the corresponding values for the control ($\eta/\eta_{H_2O} = 1$).

BV and *E. coli* motility along walls.

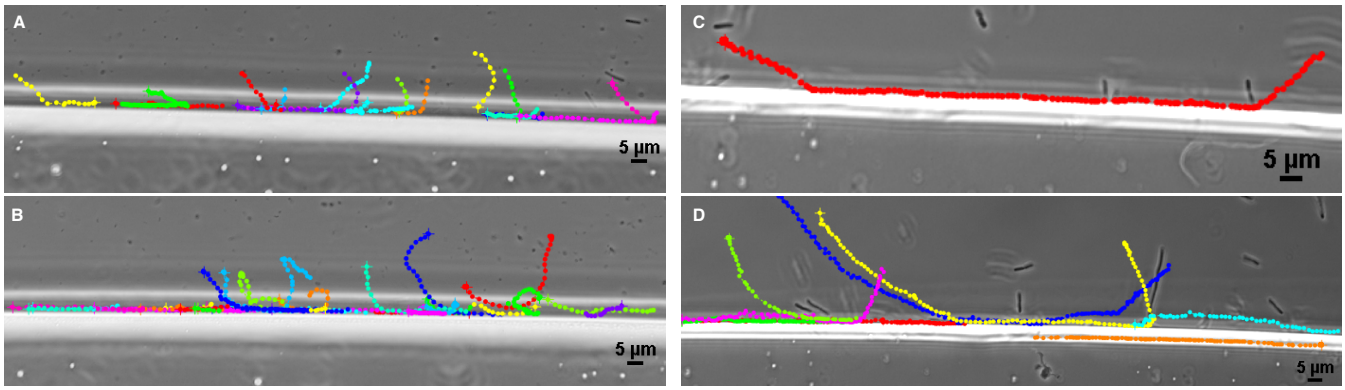

FIGURE S5. BV and *E. coli* move in straight trajectories along the walls. The wall is constructed according to the recipe provided in Materials and Methods. Healthy BV or *E. coli* solutions were then introduced against the edge of the wall. Sample BV (A and B) and *E. coli* (C and D) trajectories are shown with the bacteria swimming in (almost) straight lines along the edges of hard walls. Their behavior near walls motivated our study of the behavior near beads.

BV motility around electrically inert beads with varying radii.

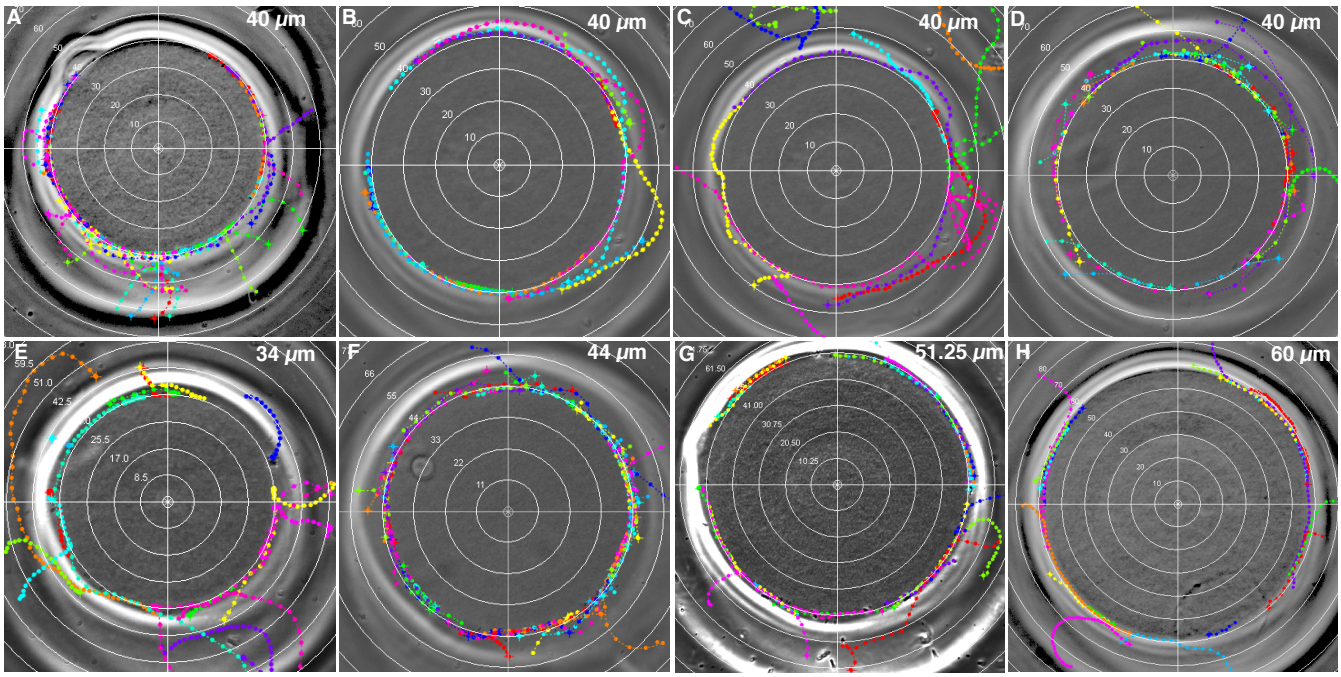

FIGURE S6. BV orbit around inert and electrically neutral beads of various radii. Here we show sample trajectories of BV around inert CL beads with radii ranging from $34 - 60\mu m$ (the density analysis we discuss in the next figure sets error bars of about $1 - 2\mu m$ on these sizes). We show sample trajectories demonstrating BV orbit around different beads with the same radii ($40\mu m$) (A to D), and for beads with varying radii ($34 - 60\mu m$) (E to H). The grid steps are as follows: (A to D) $10.00\mu m$, (E) $8.50\mu m$, (F) $11.00\mu m$, (G) $10.25\mu m$, and (H) $10.00\mu m$.

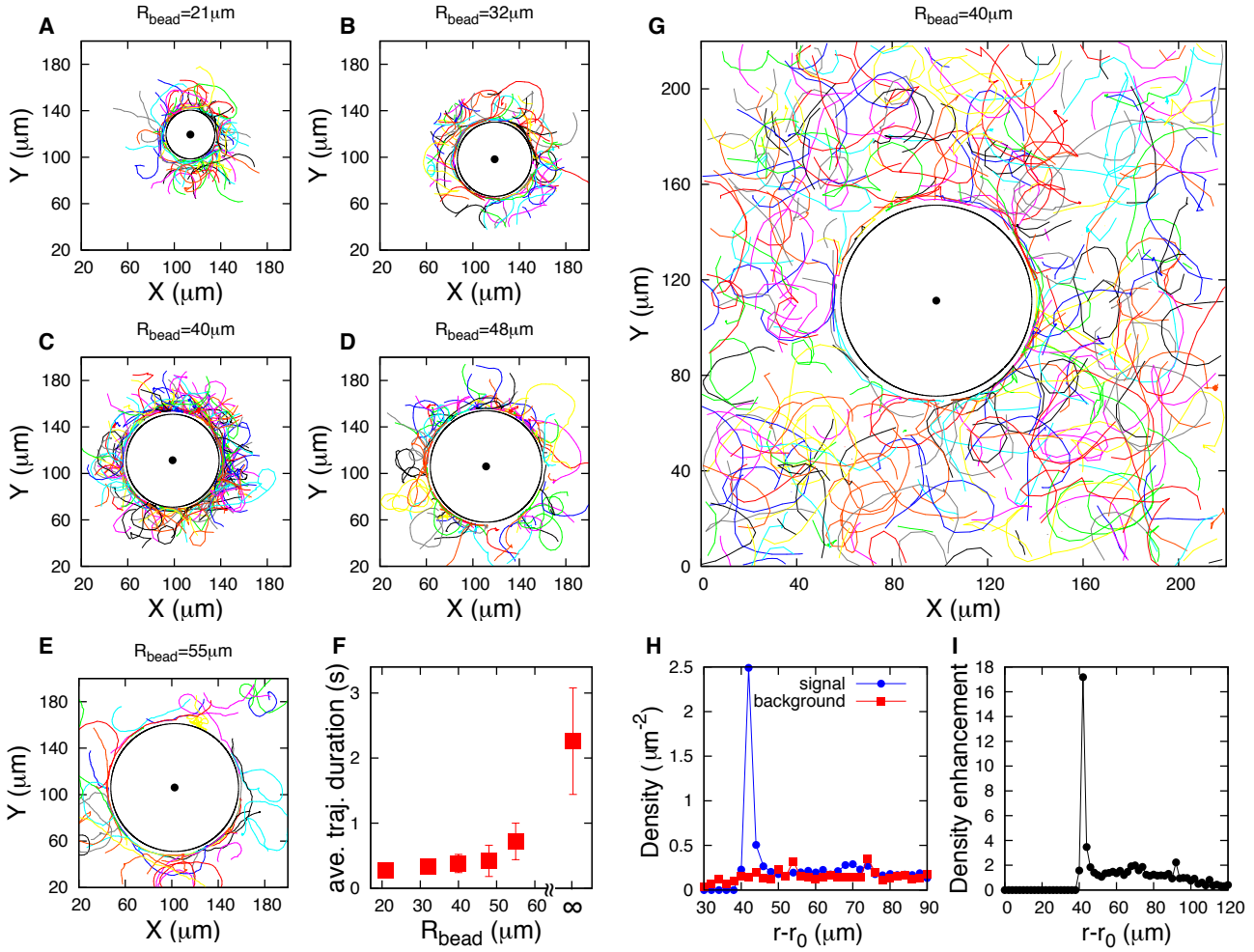

FIGURE S7. BV orbit and localize around inert and electrically neutral beads of various radii. The capture time around beads increases along with the bead radius. Here we show sample trajectories demonstrating BV orbiting and localizing around inert CL beads with radii ranging from $21-55\mu m$ (A to E). Total number of trajectories analyzed in (A to E) are 80, 119, 149, 80, and 51, respectively, and they are tracked within an area of $20\mu m$ from the bead surface (the central dot shows bead center). Mean capture time – defined as the average duration of the trajectories within $5\mu m$ from each bead surface – increases with the bead radius (F) where the data point at $R_{bead}=\infty$ shows average trajectory durations on the surface of the coverslip and slide (from Fig. **??**, B and D), as an upper limit of an infinite radius bead. For each data point, 5% of outliers are dropped from each side since long dwells indicate bacteria are stuck to surfaces while short dwells are associated with trajectories grazing, but never being captured, by beads. In (G) we show 333 BV trajectories tracked everywhere around the bead with their density profile in (H). Red line with squares in (H) represents the background density, which is the sum of densities calculated with respect to the four corner points in (G), while the blue line with filled circles is density with respect to bead center. In (I) we show the density enhancement which is the density with respect to the bead center (blue in H) divided by the average background density (red in H).

BV motility around electrically charged beads.

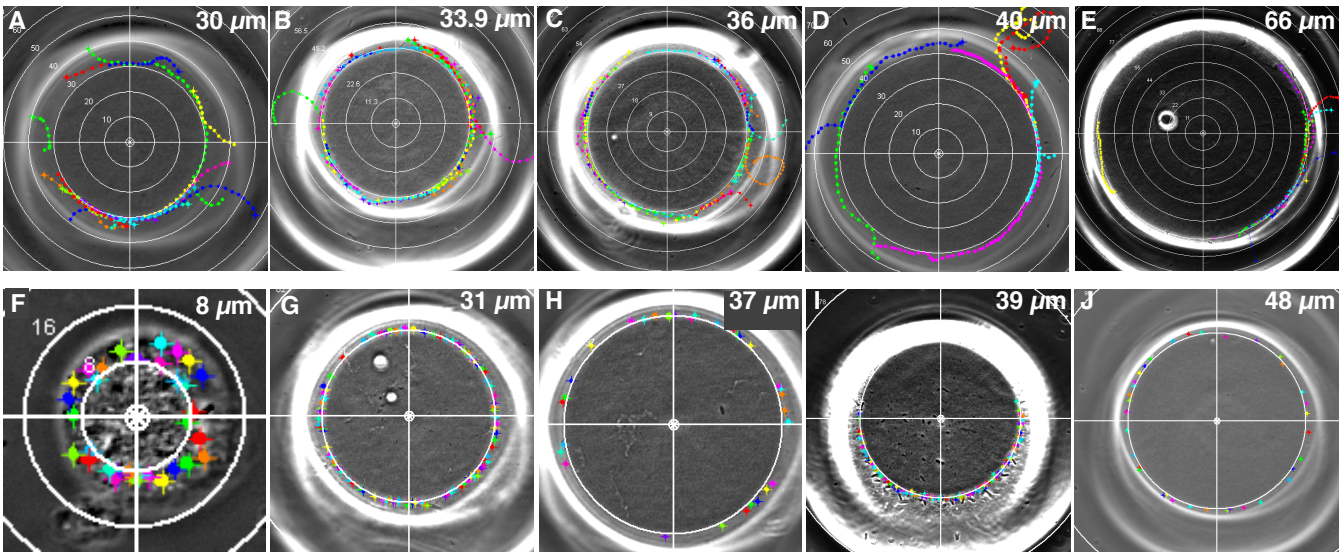

FIGURE S8. BV localize and orbit around slightly negatively-charged SP beads, while they accumulate and lose motility around positively-charged DEAE beads. Since bacteria have electrically charged membranes, geometric capture could be due to favorable electrostatic interaction between BV and the bead. For this reason, we studied the interaction of the predator as well as prey with electrically charged beads. We used electrically positive DEAE beads and electrically negative SP beads – see Materials and Methods – with different radii and we studied BV's and *E. coli*'s motility around them. The results are shown here for BV, and in the next figure (Fig. S9) for *E. coli*. The behavior of the predator is similar to that of the prey around each bead. Both circle around negatively-charged beads, although the capture strength is weaker compared to inert beads because the electrical repulsion cancels out a portion of the hydrodynamic attractive force. On the other hand, they both accumulate and stick around positively-charged beads. In this case, both the electrostatic attraction and hydrodynamic forces attract BV to the surface of the bead. Thus, numerous bacteria stick to the bead surface and lose mobility immediately after mixing beads and bacteria. Typical BV trajectories are shown around negatively-charged SL beads in (A to E), for beads with radii ranging from $30-66\mu m$. In (F to J) we show BV electrostatically trapped on positive DEAE beads with radii as small as $8.00\mu m$ up to approximately $50.00\mu m$. The radius for each bead is given on each figure. The grid steps are as follows: (A) $10.00\mu m$, (B) $11.30\mu m$, (C) $9.00\mu m$, (D) $10.00\mu m$, (E) $11.00\mu m$, (F) $8.00\mu m$, (G) $31.00\mu m$, (H) $37.00\mu m$, (I) $39.00\mu m$, and (J) $48.00\mu m$.

E. coli motility around electrically charged beads.

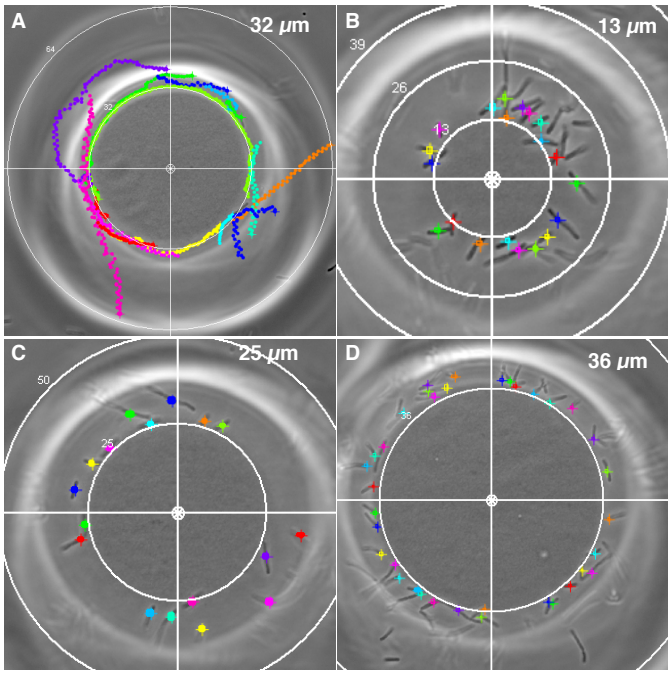

FIGURE S9. *E. coli* localize and orbit around negatively-charged SP beads, while they become electrostatically trapped and lose motility around positively-charged DEAE beads. We show sample *E. coli* trajectories around a negatively-charged bead of approximate radius $32\mu m$ (A). In (B to D), we show trapped *E. coli* cells on the surfaces of the positively-charged beads with radii $13.00\mu m$ to $36.00\mu m$. The radius for each bead is given on each figure. The grid steps are as follows: (A) $32.00\mu m$, (B) $13.00\mu m$, (C) $25.00\mu m$, (D) $36.00\mu m$.

Supporting Movies

Movie S1. BV on coverslip

In this video we show BV's motility on the coverslip surface. Solution containing BV is sandwiched between a coverslip and a microscope slide. The view is from the coverslip. The same video is shown in two panels; left panel without tracks, right panel with tracks.

Movie S2. BV in midplane

In this video we show BV's motility in the midplane between coverslip and slide. Solution containing BV is sandwiched between a coverslip and a microscope slide. The view is from the coverslip. The same video is shown in two panels; left panel without tracks, right panel with tracks.

Movie S3. BV on slide

In this video we show BV's motility on the slide surface. Solution containing BV is sandwiched between a coverslip and a microscope slide. The view is from the coverslip. The same video is shown in two panels; left panel without tracks, right panel with tracks.

Movie S4. BV on CL bead

In this video we show BV orbiting around an inert and electrically neutral CL bead (resting on the coverslip). Solution containing BV (mixed with beads) is sandwiched between the coverslip and the microscope slide. The view is from the coverslip.

Movie S5. *E. coli* on CL bead

In this video we show *E. coli* orbiting around an inert and electrically neutral CL bead (resting on the coverslip). Solution containing *E. coli* (mixed with beads) is sandwiched between the coverslip and the microscope slide. The view is from the coverslip.

References

1. Spagnolie, S. E., and E. Lauga. 2012. *Hydrodynamics of self-propulsion near a boundary: predictions and accuracy of far-field approximations. J. Fluid Mech.* 700:105-147.

2. Spagnolie, S. E., G. R. Moreno-Flores, D. Bartolo, E. Lauga. 2015. Geometric capture and escape of a microswimmer colliding with an obstacle. *Soft Matter.* 11:3396-3411.

3. Gabel, C. V., and H. C. Berg. 2003. The speed of the flagellar rotary motor of *Escherichia coli* varies linearly with protonmotive force. *Proc. Nat. Acad. Sci. USA* 100:8748-8751.

4. Qian, C., C. C. Wong, S. Swarup, and K.- H. Chiam. 2013. Bacterial tethering analysis reveals a run-reverse-turn mechanism for *Pseudomonas* species motility. *Am. Soc. Microbiol.* 79:4734-4743.

5. Swindells, J. F., C. F. Snyder, R. C. Hardy, and P. E. Golden. 1958. Viscosities of sucrose solutions at various temperatures: Tables of recalculated values. *Supplement to National Bureau of Standards Circular.* 440:1-7.